

Acoustic scattering from an aluminum cylinder in contact with a sand sediment: Measurements, modeling, and interpretation

Kevin L. Williams, Steven G. Kargl, Eric I. Thorsos
*Applied Physics Laboratory, College of Ocean and Fishery Sciences,
University of Washington, Seattle, WA 98105 USA*

David S. Burnett, Joseph L. Lopes
Naval Surface Warfare Center, Panama City Division, Panama City, FL 32407 USA

Mario Zampolli
*TNO Defense, Security and Safety, Oude Waalsdorperweg 63,
P. O. Box 96864, 2509 JG The Hague, Netherlands*

Philip L. Marston
Department of Physics and Astronomy, Washington State University, Pullman, WA 99164 USA
(Dated: October 8, 2009)

Understanding acoustic scattering from objects placed on the interface between two media requires incorporation of scattering off the interface to the object as well as the reciprocal process of scattering from the object onto the interface. In addition, the contact of the target with the interface may change the dynamics of the target. Here, this class of problems is studied in the particular context of a 61 cm long, 30.5 cm diameter aluminum cylinder placed on a flattened sand interface. Experimental results are presented for the monostatic scattering from this cylinder for azimuthal scattering angles from 0 to 90 degrees and frequencies from 1 to 30 kHz. These results are presented both in terms of the absolute target strength measured as a function of azimuthal angle and frequency and in terms of Synthetic Aperture Sonar (SAS) images derived from these same data. Next, details seen within these experimental results are explained using physical acoustics derived insight. Subsequently, the target strength results are compared to finite element calculations that incorporate the geometry and interface/target interactions at various levels of sophistication. The simplest calculation assumes that the source and receiver are at infinity and uses the finite element result for the cylinder in free space along with image cylinders for approximating the target/interface interaction. Then the effect of moving the receiver to a finite distance and inclusion of a more complete Green's function for the target/interface interaction is examined. These first two calculations use the axial symmetry of the cylinder in carrying out the analysis, i.e., the result is a three dimensional prediction for scattering derived using multiple two dimensional calculations. Finally, the results from a three dimensional finite element analysis are presented and compared to both the experiment and the axially symmetric calculations.

I. INTRODUCTION

Scattering from elastic objects placed on or near the water/sediment interface is a problem receiving increasing attention¹⁻⁵. In many cases the targets of interest have been hollow spheres. This focus on spheres has been, in part, because numerical and analytical modeling of the target is well-developed, thus one can concentrate on the physics introduced by being near the sediment/water interface. However, recent developments in finite element modeling^{5,6} now allow examination of more complicated elastic objects placed on the interface between two media.

In this article the target examined is an aluminum cylinder with flat ends. The cylinder is 61 cm long and 30.5 cm in diameter. It was placed on a flat sand/water interface (often called the “proud” target case, a terminology that will be used here) and data acquired at frequencies from 1 to 30 kHz over azimuthal angles from 0° (broadside) to 90°. Like the sphere, examination of scat-

tering from finite elastic cylinders in the free field also has a long history from which the physical processes involved in the scattering can be quantitatively understood⁷⁻¹⁰. This insight is valuable for the present case when examining experimental results and when comparing finite element modeling to these experimental results.

There are three goals in the present article. The first is to present experimental results for the absolute target strength of the proud cylinder as well as SAS images of the cylinder. These results are important for testing models not only within the rest of this article but hopefully also for models developed by other researchers. The second goal is to explain the experimental results within the context of previous physical acoustics analyses^{9,10}. The final goal is to use data/finite element model comparisons and the physical acoustics insights to better understand the essential physical processes and geometrical parameters that must be included in finite element modeling in order to predict the absolute target strength of a proud cylinder for the geometries realized here.

The remainder of this article is organized as follows.

Report Documentation Page			Form Approved OMB No. 0704-0188		
Public reporting burden for the collection of information is estimated to average 1 hour per response, including the time for reviewing instructions, searching existing data sources, gathering and maintaining the data needed, and completing and reviewing the collection of information. Send comments regarding this burden estimate or any other aspect of this collection of information, including suggestions for reducing this burden, to Washington Headquarters Services, Directorate for Information Operations and Reports, 1215 Jefferson Davis Highway, Suite 1204, Arlington VA 22202-4302. Respondents should be aware that notwithstanding any other provision of law, no person shall be subject to a penalty for failing to comply with a collection of information if it does not display a currently valid OMB control number.					
1. REPORT DATE 10 AUG 2009		2. REPORT TYPE Final Technical		3. DATES COVERED 00-11-2005 to 00-12-2008	
4. TITLE AND SUBTITLE Acoustic scattering from an aluminum cylinder in contact with a sand sediment : Measurements, modeling, and interpretation			5a. CONTRACT NUMBER N00014-01-G-0460/D.O. 0043		
			5b. GRANT NUMBER		
			5c. PROGRAM ELEMENT NUMBER		
6. AUTHOR(S) Kevin Williams; Steven Kargl; Eric Thorsos; David Burnett; Joseph Lopes			5d. PROJECT NUMBER		
			5e. TASK NUMBER		
			5f. WORK UNIT NUMBER		
7. PERFORMING ORGANIZATION NAME(S) AND ADDRESS(ES) Applied Physics Laboratory, 1013 N.E. 40th St., Box 355640, Seattle, WA, 98105-6698			8. PERFORMING ORGANIZATION REPORT NUMBER		
9. SPONSORING/MONITORING AGENCY NAME(S) AND ADDRESS(ES) Office of Naval Research, 875 North Randolph St., Arlington, VA, 22203-1995			10. SPONSOR/MONITOR'S ACRONYM(S) ONR		
			11. SPONSOR/MONITOR'S REPORT NUMBER(S)		
12. DISTRIBUTION/AVAILABILITY STATEMENT Approved for public release; distribution unlimited					
13. SUPPLEMENTARY NOTES					
14. ABSTRACT Understanding acoustic scattering from objects placed on the interface between two media requires incorporation of scattering off the interface to the object as well as the reciprocal scattering process. In addition, the contact of the target with the interface may change the dynamics of the target. This class of problems is studied in the particular context of an aluminum cylinder placed on a flattened sand interface. Experimental results are presented for the monostatic scattering from this cylinder for azimuthal scattering angles from 0 to 90 degrees and frequencies from 1 to 30 kHz. Next, details seen within these experimental results are explained using physical acoustics derived insight. Subsequently, target strength results are compared to finite element calculations that incorporate the geometry and interface/target interactions at various levels of sophistication. The simplest calculation assumes that source and receiver are at infinity and uses the finite element result for the cylinder in free space along with image cylinders for approximating the target/interface interaction. Then the effect of moving the receiver to a finite distance and inclusion of a more complete Green's function for the target/interface interaction is examined. The result is a three-dimensional prediction for scattering derived using multiple two dimensional calculations.					
15. SUBJECT TERMS acoustic target scattering, target strength, finite element modeling, bistatic scattering					
16. SECURITY CLASSIFICATION OF:			17. LIMITATION OF ABSTRACT Same as Report (SAR)	18. NUMBER OF PAGES 12	19a. NAME OF RESPONSIBLE PERSON
a. REPORT unclassified	b. ABSTRACT unclassified	c. THIS PAGE unclassified			

Section II presents a summary of the experimental apparatus and procedure as well as the analyzed results. Section III examines the experimental results using a process oriented view derived via physical acoustics. Section IV then describes a series of finite element calculations with increasing fidelity relative to the actual experimental arrangement and the sediment/target interaction, and compares those results to the data. Section V summarizes. A subset of the author list concentrated on the work presented in particular sections. Section II documents the experiment and data analysis carried out by K LW, EIT, SGK, and JLL. Section III was the focus for PLM. Sections IV A, IV B, and IV C were written by, and present the analyses of, K LW, MZ, and DSB, respectively.

II. EXPERIMENT

The experiment described here was carried out in March 2008 in the Naval Surface Warfare Center test facility 383 in Panama City, Florida. The test facility includes a fresh water pool 110 m long by 80 m wide with 1.5 m of sand on the bottom. The water depth above the sand is approximately 14 meters. The built-in filtration system allows 10 m dive visibility.

A. Apparatus and procedure

The measurement system used was designed to carry out backscattering measurements with sufficient spatial resolution to perform Synthetic Aperture Sonar (SAS). Figure 1 shows an engineering drawing of the system. It comprises a bottom-mounted rail and a rail tower instrumented with transducers and position sensors. The rail is deployed by divers in sections, each rail section is 7 m in length. Rail sections are connected and leveled to form longer rail lengths; during the experiment 3 sections were used. The electric motor-driven tower traversed the rail at a constant speed of 5 cm/s. Transmissions were made twice per second as the tower moved along the rail; given the horizontal width of the receiver (10 cm) this transmission rate is sufficient for SAS processing.

The electronics controlling transmission, data acquisition and digitization, tower motion and monitoring of all position instrumentation (e.g., inclinometers, pressure sensors) resides in a tower-mounted electronics housing. Separate power and data/control cables are connected to this housing. These cables are attached to a triangle shaped guide at the backside of the tower to assure that the cables are not pinched as the tower moves. These cables were fed back to a mobile office where topside experimental control resided. Thus, data analysis could be carried out as the experiment proceeded and experiments altered based on those results.

The transmitted pulse used was a 6 ms FM slide from 1 to 30 kHz. The beamwidth of the transmitter is broad over the entire frequency range (full width greater than

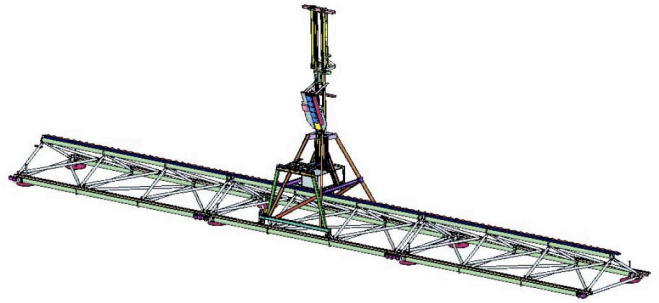


FIG. 1:

Rail and mobile tower system used. In the figure, the rail consists of 3 rail sections each 7 m in length, resulting in a 20 m span over which the tower could be moved.

40°) in order to allow SAS processing. The receiver contains six separate elements arranged in a vertical array, and each receive element has a 10 cm horizontal aperture. The vertical apertures are (from top to bottom) 30, 10, 10, 10, 10, and 30 cm. Backscattering signals received on each element are recorded separately. This allows the vertical beam pattern to be altered to minimize scattering interference from the water/air boundary. It also allows time delay between separated receiver elements to be used to determine the depression angle of target returns relative to the center of the receive beampattern. Both source and receiver were calibrated as a function of frequency before the experiment to allow backscattered pressure to be determined in absolute units of dB re 1 μ Pa with an uncertainty of approximately ± 1 dB.

The transmitter and receiver are mounted on a panel that can be rotated up or down in five degree increments. For the measurements presented here the inclinometer mounted on this panel indicated a tilt angle of 20.3° relative to the vertical. This angle plus the arrival time of the specular reflection from the cylinder to the receive elements allowed the geometry to be determined to an uncertainty of approximately 5 cm. At the point of closest approach, the horizontal distance from the center of the transmitter (receiver array) to the center of the cylinder (deployment discussed below) was 9.55 (9.45) m. The center of the transmitter (receive array) was 3.60 m (3.85 m) above the center of the cylinder. From these measurements the grazing angle for the ray drawn from transmitter (receive array) center to cylinder center was 20.7° (22.2°).

The aluminum cylinder was deployed by divers approximately 10 m from the center of the rail. Before deployment of the cylinder, the sand in a 3 m (range) by 2 m (cross range) area was flattened by divers using two I-beams deployed in the sand and a third I-beam used as a scrapper. After this operation the I-beams were removed and the cylinder deployed using a lift system that consists of a flotation bladder and built-in winch with wireless electronic control from shore. This system, along with an

underwater communication system between divers and winch operator, allowed divers to remain neutrally buoyant above the flatten area while placing the cylinder at the designated location and orientation. Small lift lines from which the cylinder was suspended were removed, leaving only a small indentation (1 to 2 cm long and a few millimeters deep at two locations along the cylinder). The results shown here are from four deployments with associated orientations of the center line of the cylinder relative to the path of the rail tower of 0° (broadside), 25° , 47° , and 70° . For each cylinder orientation the tower traversed the entire length of the rail transmitting 800 times.

The sound speed in the (fresh) water was determined from its temperature to be 1486 m/s. The water (sand) density was assumed to be 1000 (2000) kg/m³. The sound speed in the sediment, measured using a diver deployable measurement system¹¹, was 1694 m/s. This same system enables sediment attenuation (given here in terms of δ_p , the ratio of the imaginary to real wavenumber¹²) to be determined. δ_p was 0.008. Finally, the material parameters used for the aluminum cylinder were density = 2700 kg/m³, longitudinal sound speed = 6568 m/s, and shear speed = 3149 m/s. Radiation damping dominates inherent attenuation for the waves within the cylinder that lead to measurable backscatter, and the finite element results to be presented are thus not sensitive to attenuation values chosen; however, for completeness, the results shown here assumed 0.00015 dB/m/kHz for the longitudinal wave and 0.0003 dB/m/kHz for the shear wave.

B. Results

Figure 2 presents the backscattering from the proud cylinder for the four different orientations. The scale is in dB relative to the brightest pixel in each panel. There is a rich structure of returns for all orientations. One goal in the remainder of the article is to understand this structure and to quantitatively compare finite element modeling results to the data. In this regard, further analysis of these data will be useful.

The data were SAS processed to obtain the images shown in Fig. 3. The four panels coincide with the same panels in Fig. 2. The dB scale is again relative to the brightest pixel in each panel. The broadside SAS image (Fig. 3(a)) clearly indicates the length of the cylinder. The obvious multiple return structure in Fig. 3(a) as well as other features seen in panels of Figs. 2, 3 and in Fig. 4 below will be identified in Sec. III.

The data were also processed to get absolute levels for the target strength of the proud cylinder as a function of azimuthal angle and frequency. The normalizing pressure is the value of the transmitted pressure at the location of the center of the cylinder in the absence of both the cylinder and the sand (i.e., in the free field). The result is shown in Fig. 4. The azimuthal angle is measured

on the horizontal plane through the axis of the cylinder relative to broadside. Thus 0° is broadside and 90° is end-on as seen by an observer at the center of the rail 0.15 m above the water-sand interface. Figs. 5, 6, 7, 8, and 9 are results of finite element calculations using different assumptions. They will be discussed in detail in the later sections but are grouped together with the experimental results to facilitate comparisons.

III. PHYSICAL ACOUSTICS INTERPRETATION

Above 16 kHz ($ka \approx 10$) it is helpful to consider coupling conditions for the free field excitation of elastic waves guided by the surface of the cylinder^{9,10}. Prior calculations of the phase velocity of high-frequency modes propagating down infinitely-long solid steel cylinders in water give values close to the speed of a Rayleigh wave on an elastic half space¹³. Calculations for an infinitely-long aluminum cylinder yield a similar result¹⁴. A noteworthy difference between aluminum and steel cylinders is that the rates of radiation damping for most axially propagating modes on aluminum cylinders are over twice that for similar modes on steel cylinders as a consequence of the smaller density of the aluminum¹⁵. This increase in radiation damping broadens the range of cylinder tilt angles over which the modes are excited^{14,15}.

For the purpose of describing the coupling, it is convenient to consider free field ensonification by a plane wave having a wave vector \mathbf{k}_i . The plane containing the unit vector $\hat{\mathbf{k}}_i$ and a unit vector along the cylinder's axis $\hat{\mathbf{z}}_{cyl}$ intersects the side of the cylinder closest to the source along a meridian of the cylinder. The excitation of high-frequency elastic waves propagating along the meridian is governed by the value of the tilt angle^{9,13} $\gamma = \arcsin(\hat{\mathbf{k}}_i \cdot \hat{\mathbf{z}}_{cyl})$ relative to the Rayleigh wave coupling angle $\gamma_R = \arcsin(c/c_R)$ where c is the speed of sound in water and c_R is the Rayleigh wave velocity. For aluminum in water $\gamma_R \approx 30^\circ$. Experiments with metal cylinders having flat ends show that the backscattering is enhanced when γ is close to γ_R as a consequence of radiation associated with elastic meridional rays which have reflected off the end of the cylinder^{9,14}. When γ is decreased below γ_R , sufficiently long cylinders display backscattering features associated with the excitation and reflection of helical rays by the end of the cylinder^{8-10,14}.

To compare the expected high-frequency behavior with features visible in Figs. 2-4, notice that γ is related to the grazing angle θ_g and the cylinder's azimuthal orientation angle ϕ by $\gamma = \arcsin(\cos \theta_g \sin \phi)$. See Eq. (A6). In Fig. 2(b) and 3(b), ϕ is 25° so that γ is 23° and the back end of the cylinder appears bright (i.e., in Fig. 3(b), the complex structure at a cross range from about -0.4 to 0.1 m and a range of about 0.1 to 0.2 m). This is interpreted as a consequence of radiation by elastic meridional and helical rays excited on the cylinder and reflected off of

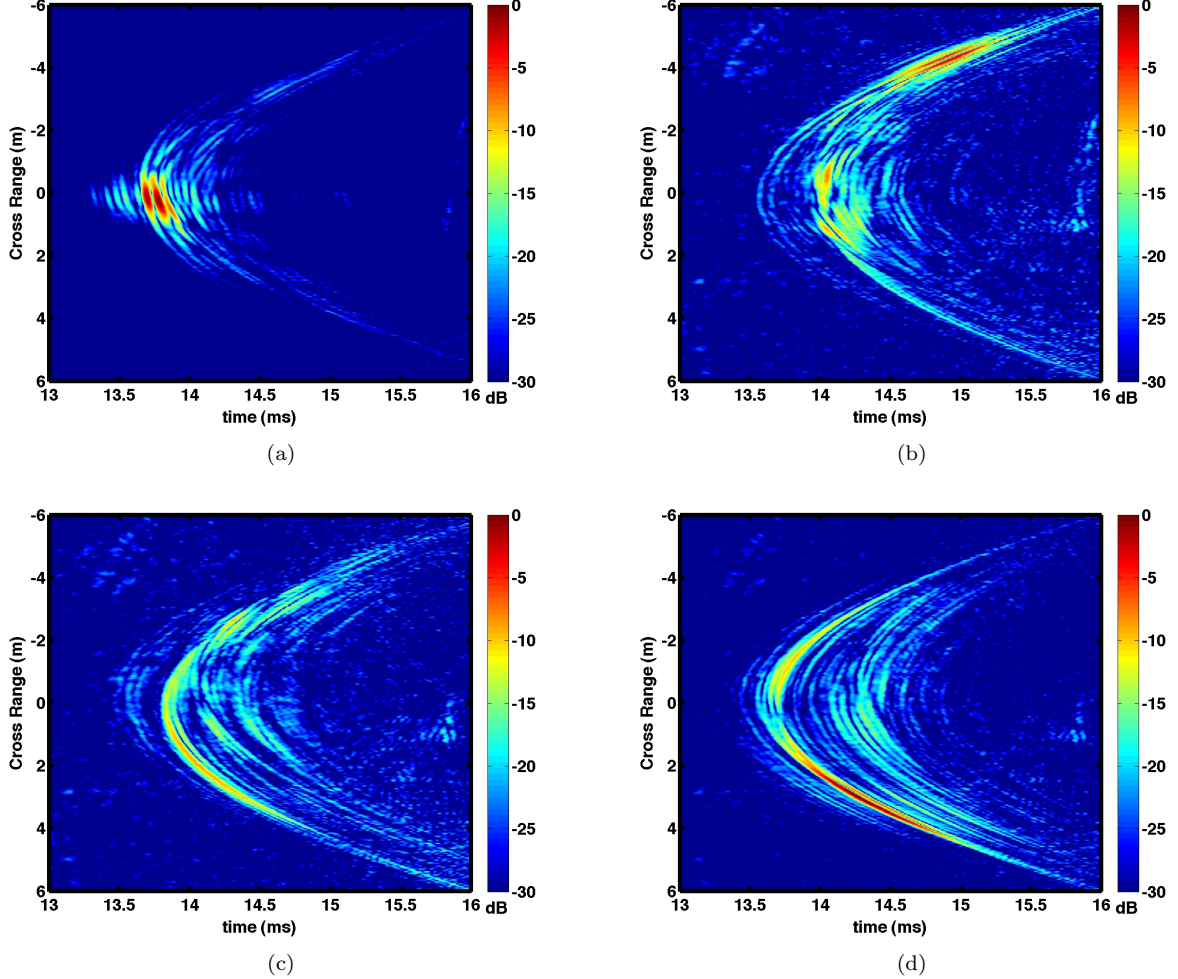


FIG. 2: Each panel shows pulse compressed and basebanded backscattering returns for a proud 60 cm long aluminum cylinder for 480 transmissions as the rail tower translated the central 12 meters of the rail. The cylinder's orientation is different in each panel. The axis of the cylinder relative to the path of the rail tower for each case is a) 0° (broadside), b) 25° , c) 47° , and d) 70° . The dB scale is relative to the brightest pixel in each panel.

the far end of the cylinder. The corresponding region in Fig. 2(b) is from a cross range of about -1 to 1 m.

In Figs. 2(c) and 3(c), ϕ is 47° so that γ is 43° . The aforementioned backscattering enhancements are suppressed and the magnitude of the scattering associated with the far end of the cylinder is greatly reduced. A corresponding reduction in free field backscattering for mid-range values of γ has been observed for steel^{9,10} and aluminum¹⁴ cylinders.

In Figs. 2(d) and 3(d), ϕ is 70° so that γ is 61° . This γ is close to the predicted value of $90^\circ - \gamma_R \approx 60^\circ$ associated with the excitation of a face-crossing Rayleigh wave on the near flat end of the cylinder¹⁰. When the excited wave reflects from the curved edge of the cylinder, the radiation from the reflected Rayleigh wave is directed toward the source of the sound. In agreement with that interpretation the end of the tilted cylinder closest to the source appears brightest in Figs. 2(d) and 3(d).

The aforementioned features are also visible in the high frequency structure in Fig. 4 where the vertical axis gives the cylinder's apparent azimuthal orientation angle ϕ . The face-crossing enhancement is most noticeable above 19 kHz ($ka \approx 12$), which is consistent with free field observations for steel¹⁰ and aluminum¹⁴ cylinders. The meridional-ray feature near $\phi \approx 32^\circ$ ($\gamma \approx 30^\circ$) is suppressed below 15 kHz. The features are also visible in the the finite element results discussed in Sec. IV. Below 10 kHz some enhancements are visible associated with the coupling of sound with specific resonances of the truncated cylinder. A noticeable example is the feature near $\phi = 50^\circ$ and 7 kHz in Fig. 4.

The complications introduced by the proximity of the cylinder to the sediment are most easily seen in Fig. 3(a) where the specular echo is split into a triplicate of features associated with paths discussed in Sec. IV A. That splitting is consistent with a ray analysis of reflections

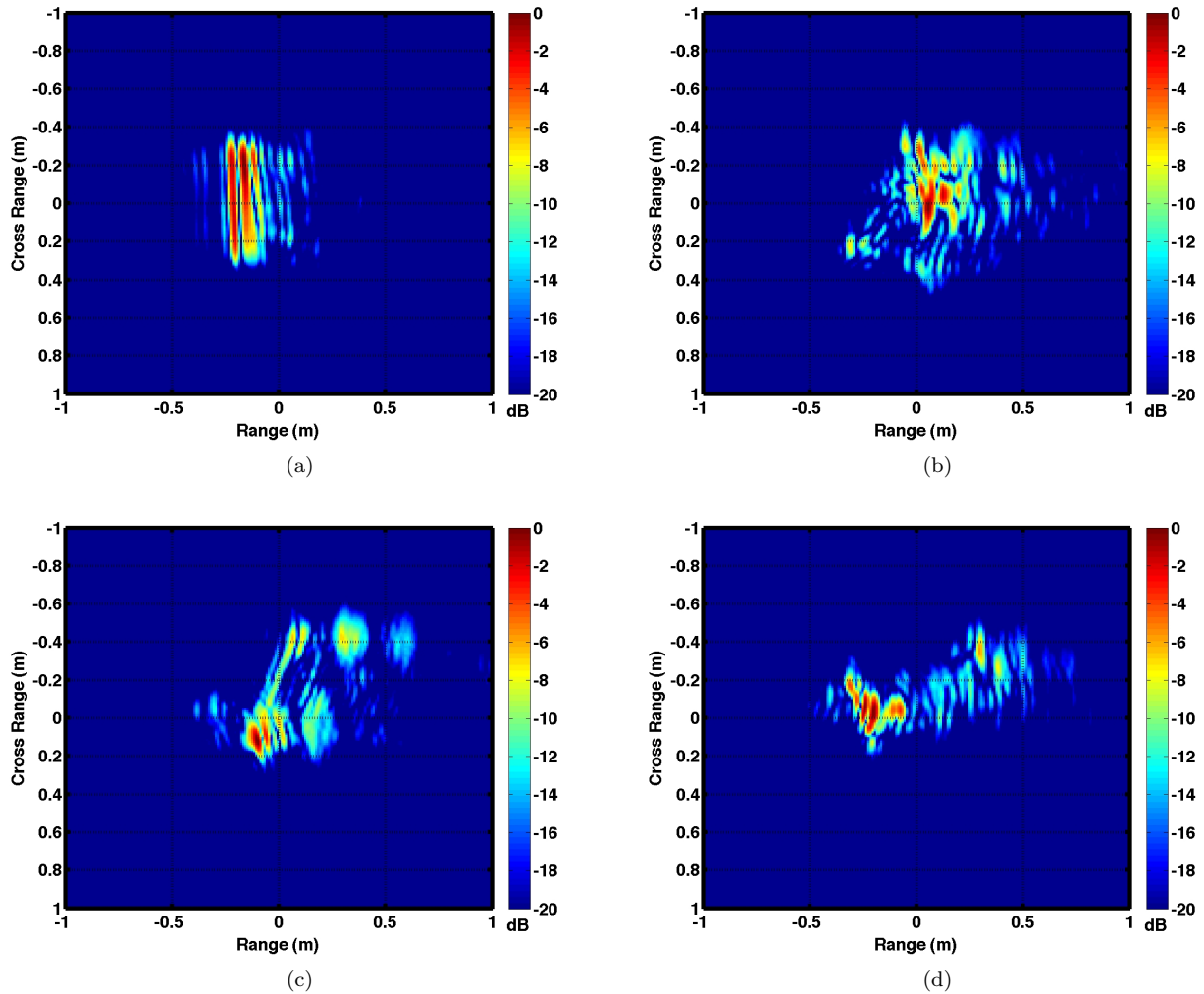


FIG. 3: The SAS images of the proud 60 cm long cylinder resulting from processing the data presented in Fig. 2. The dB scale is relative to the brightest pixel in each panel. Note that range 0 in the figure is relative to 9.5 m - the nominal horizontal distance from transmitter/receiver array to the center of the cylinder.

from cylinders and a flat adjacent surface given by Baik and Marston^{14,16}.

IV. FINITE ELEMENT MODELING

Finite element modeling of the proud cylinder's target strength is presented within this section. The results from three separate calculations are shown. Each calculation incorporates the geometry and interface/target interactions at a different level of fidelity. The simplest calculation (Sec. IV A) assumes that the source and receiver are at infinity and uses the finite element result for the cylinder in free space along with image cylinders for approximating the target/interface interaction. Then the effect of moving the receiver to a finite distance and inclusion of a more complete Green's function for the target/interface interaction is examined (Sec. IV B). These

first two calculations use the axial symmetry of the cylinder in carrying out the analysis^{5,6}, i.e., the result is a three dimensional prediction for scattering derived using multiple two dimensional calculations. Finally, the results from a three dimensional finite element analysis (Sec. IV C) is presented and compared to both the experiment and the axially symmetric calculations.

A. Source/receiver at infinity and image cylinder approximation

This most approximate finite element calculation assumes the source and receiver are far enough away to use plane wave approximations, uses the results calculated for the cylinder in the free field, and includes the effect of the interface via image cylinders. This allows the use of plane wave, finite element results calculated using the

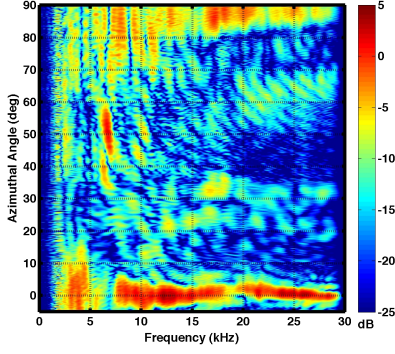


FIG. 4:

Experimental result for the absolute target strength of the proud cylinder as a function of azimuthal angle and frequency.

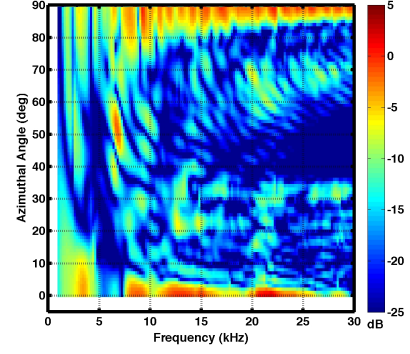


FIG. 7:

Finite element result for absolute target strength of the proud cylinder. Result calculated using actual experiment geometry and with second order accurate layered medium Green's functions (see Sec. IV B for details).

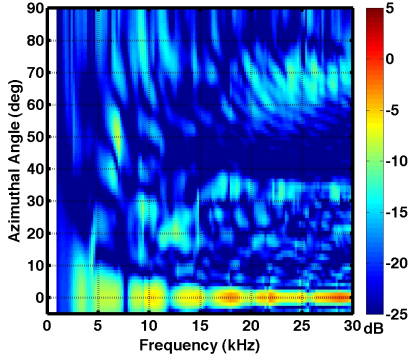


FIG. 5:

Finite element result for absolute target strength of the free field cylinder as a function of azimuthal angle and frequency. Result calculated assuming source and receiver at infinity (see Sec. IV A for details).

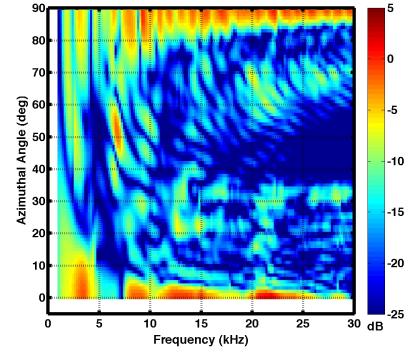


FIG. 8:

Finite element result for absolute target strength of the proud cylinder. Result calculated using actual experiment geometry and with first order accurate layered medium Green's functions (see Sec. IV B for details).

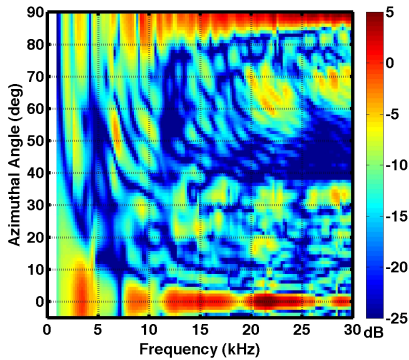


FIG. 6:

Finite element result for absolute target strength of the proud cylinder as a function of azimuthal angle and frequency. Result calculated assuming source and receiver at infinity and using image cylinders to account for cylinder/interface interactions (see Sec. IV A for details).

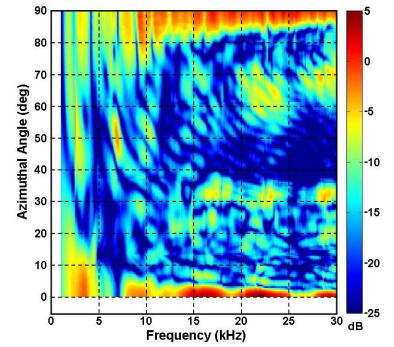


FIG. 9:

3-D FE computation of absolute target strength of the proud cylinder as a function of azimuthal angle and frequency. (see Sec. IV C for details).

axial symmetry of the cylinder in the freefield. This can have a computational advantage since the freefield result

can be determined via multiple 2-D calculations instead of a full 3-D calculation. Figure 10 shows the paths taken into account and the image cylinders. The figure is oriented such that the observer is looking down the cylinder axis but the paths shown should be viewed as projections of the paths for any incident direction onto this plane. Several facts can be immediately discerned from the figure. First, the paths labeled 2 and 3 represent bistatic scattering paths even though the source and receiver are arranged in a monostatic geometry. Second, paths 2, 3 and 4 are delayed relative to path 1 in arriving to the receiver. The phase delay of paths 2 and 3 in arriving to the receiver relative to path 1 is $2ka \sin \theta_g$ and the delay of path 4 is $4ka \sin \theta_g$ (k is wavenumber, a is the cylinder radius and θ_g is the grazing angle onto the sediment) regardless of the azimuthal rotation of the cylinder relative to the acoustic path. However, the angle θ_{cyl} (which is the bistatic angle as measured in the cylinder coordinates) in Fig. 10 is equal to θ_g only when the cylinder is broadside to the acoustic path. For all other azimuthal orientations (angles ϕ), θ_{cyl} can be defined in terms of θ_g and ϕ . Appendix A presents the cylinder coordinates and angles ϕ_{cyl} and θ_{cyl} and derives expressions for them in terms of the relevant experiment angles θ_g and ϕ .

The backscattering target strength to be presented here is calculated as

$$TS(f, \phi, \theta_g) = 20 \log(r_r / (r_o P_o)) \quad (1)$$

$$(p_{path1} + 2R_{ws}(\theta_g) \exp(i2ka \sin \theta_g) p_{path2} + R_{ws}^2(\theta_g) \exp(i4ka \sin \theta_g) p_{path4}),$$

where r_r is the range from the center of the cylinder to the receiver, r_o is the reference range of 1 m, $R_{ws}(\theta_g)$ is the water/sediment reflection coefficient (in the present case the sand sediment was treated as a fluid), and P_o is the incident pressure at the location of the cylinder in the absence of the sediment. The 2 in the path 2 term accounts also for the reciprocal path 3.

The finite element calculation⁶ to obtain the pressures for the paths in Eq. (1) is for the cylinder in the free field. The pressures p_{path1} and p_{path4} are taken as equal and are the backscattering pressures as a function of ϕ_{cyl} (with $\theta_{cyl} = 0$). The calculation of p_{path2} has to account for the bistatic nature of that path (and path 3) and the required bistatic angle is $2\theta_{cyl}$. Thus the path 2 contribution depends on both ϕ_{cyl} and θ_{cyl} which are functions of ϕ and θ_g given in Appendix A.

There are several assumptions implicit in this calculation. The use of a single grazing angle with parallel incident and scattered angles implies the source and receiver are far enough away to assume plane wave incidence and return. (Far field geometry is also implicit in the use of r_r for all paths). It is assumed that the two fluid Green's function⁵ can be accurately approximated via use of a reflection coefficient. It also ignores any alteration of the target response due to the contact with the sediment

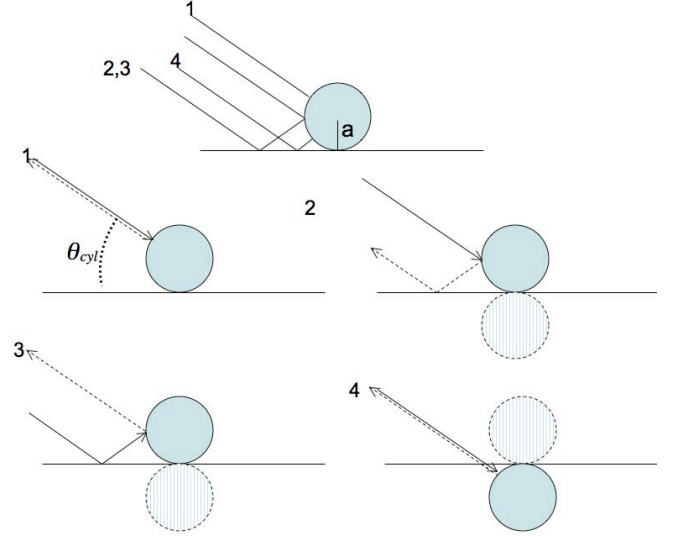


FIG. 10:

Paths included in finite element calculation in Sec. IV A. Top panel shows all paths and the bottom four panels show the separate paths. Path 2 and 3 are reciprocal and include one bottom bounce, path 4 includes two bottom bounces.

and any multiple scattering between target and interface. These assumptions are tested in subsequent subsections.

The finite element calculation used a mesh size of 2 cm. The convergence of the free field result using this mesh size was tested at the highest frequency of the calculation (30 kHz) for azimuthal angles from 0 to 90 degrees. Calculations were done for mesh sizes of 4, 2 and 1 cm. Differences as large as 2 dB were found between the 4 and 2 cm meshes. The largest difference seen between the 2 and 1 cm results was 0.2 dB. The same mesh size was used for all frequencies. This certainly increased run time dramatically but allowed a “start and forget” approach. The run time to calculate TS every 200 Hz from 1 to 30 kHz and every 1° from 0 to 90 degrees was about six days on a dual processor, 3 GHz computer.

Two results are presented. Both give absolute target strength to be compared to Fig. 4. Figure 5 shows the target strength for the cylinder in the free field. Figure 6 shows the target strength for the proud cylinder as calculated via Eq. (1) using a θ_g of 21.5° (the mean of the transmitter and receiver grazing angles).

It is immediately obvious that the free field result does not match the overall target strength measured in the experiment as well as the proud result does. Closer examination also shows that much of the detailed structure seen in the experiment is reproduced in the proud finite element calculation. However, there are also regions in frequency- ϕ space where there is significant discrepancy, e.g., for frequencies of 15 to 30 kHz with azimuthal angles from 10 to 20 degrees. This particular region has been identified in the previous section as including contributions from helical waves that have the potential to

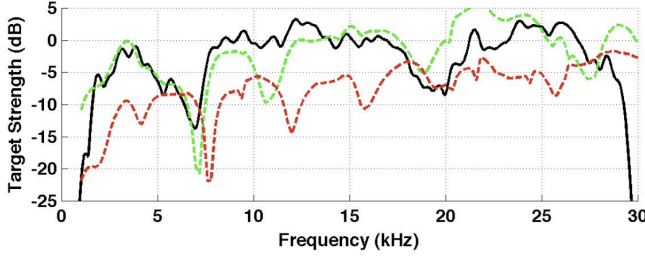


FIG. 11:

Comparison broadside target strength: data (black), free field finite element calculation (red), and proud finite element calculation (green) using Eq. (1).

be more significantly impacted by the fact the cylinder is on the sediment. The question to be examined next is to what extent more sophisticated finite element calculations improve data/model comparisons.

Before proceeding, however, it is interesting to examine the broadside ($\phi = 0^\circ$) and $\phi = 90^\circ$ results further. Figure 11 compares data and finite element results for broadside. Enhancements in target strength of up to 10 dB are seen in both the data and the proud finite element results relative to the free field case. For $\phi = 90^\circ$ the free field result is much lower than the proud data and finite element results because there is no scattering from the flat end back to the receiver. It is the single bounce paths from the end that gives the main contribution to scattering near $\phi = 90^\circ$.

B. Source and receiver at finite distance and second order approximation of the layered medium Green's function

In an attempt to address the discrepancies between the target scattering FE model results of Sec. IV A and the experimental data, the axisymmetric target scattering model is modified to include the source at a finite distance, and the vertical position of the receiver array element locations for the various positions along the rail. The source at a finite distance is modeled as a point source, which is decomposed into the azimuthal modal cosine series required by the axisymmetric target scattering model⁶ using the fast Fourier transform¹⁷. The procedure followed for taking into account the presence of the seabed is similar to the procedure represented in Fig. 10, which takes into account the first order interactions between the incident field, the target, and the seabed, neglecting higher order multiple reflections and neglecting the impedance jump at the target/fluid interface in contact with the seabed.

For a given location and orientation angle of the cylinder with respect to the rail, one determines the actual positions of the source and of the receive array element centers and the resulting incidence angle on the cylinder

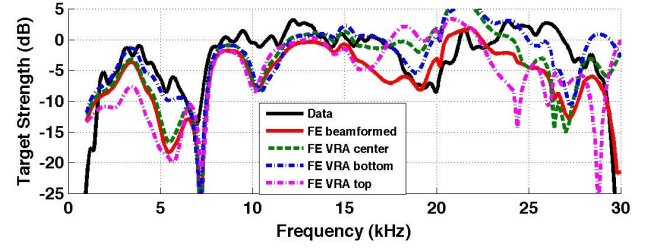


FIG. 12: Target strength as a function of frequency at broadside aspect and cylinder orientation parallel to the rail, computed by taking into account the actual source-target-receiver geometry of the experiment. Strong variations of the target strength as a function of sensor location along the vertical receive array are evident. The red curve shows the effect of applying the beamforming to the model results.

in-plane with the seafloor. The finite element computation is carried out for the signal incident directly from the source, and for the bottom reflected incident signal (image source contribution), which is multiplied by the sea floor reflection coefficient associated with the grazing angle of the ray connecting the image source and the target center. For each of the incident fields (source and image source contribution), the coordinate system is rotated into the coordinate system of the FE calculation, according to Appendix A, and the problem is solved with the FE model. In the final step, the result from each of the two FE calculations is translated back into the physical coordinate system, and the scattered field is repropagated from the target surface to the receivers using the discrete sum representation of Helmholtz-Kirchhoff integral with the approximate two-layered medium Green's function presented in Eqs. (4)–(6) of the work by Zampolli et al.⁵ This yields two target echo components at the receiver locations, one generated by the source incident field and one generated by the boundary reflected incident field (image source), which are added up coherently at each receiver.

Figure 12 shows the strong variability of the simulated target strength with receiver location, and the effect of beamforming the simulated responses at the receive array element centers. Even at the lower frequencies there are large variations between the echos at the receiver locations along the vertical array, caused by the interference between the direct and the boundary reflected echo components. Since it is beamformed data that are shown throughout the paper, in what follows below the simulated response at the array elements is beamformed by adding coherently the complex pressures computed at each of the hydrophone center locations.

The strong variability in the simulated echo, associated with small changes in the source-target-receiver geometry, is also evident in Fig. 13, which shows how a relatively minor change in the array tilt angle (just 1.3°) causes large changes in the computed target strength. Furthermore, a given source-target aspect angle can be obtained by changing the cylinder orientation, and by

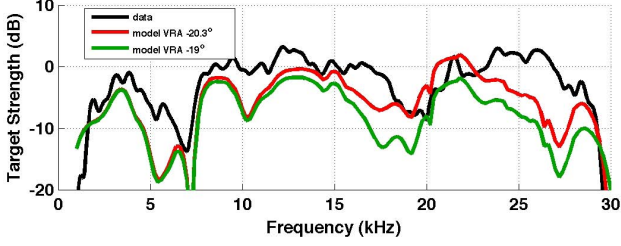


FIG. 13: Variation of the simulated beamformed array response caused by changes in the vertical receive array tilt angle.

displacing the tower along the rail. Figure 14 shows a comparison between the simulated responses computed for broadside incidence with the cylinder parallel to the rail and the tower located at the center of the rail, and with a cylinder orientation of 25° relative to the rail and the tower displaced by 4.45 m with respect to the rail center. Also in this case it can be seen that the variations in the computed response associated with changes in the geometry are not negligible.

The difference between the broadside insonification ($\phi = 0^\circ$) at 0° cylinder orientation and at 25° lies in the grazing angle, which decreases by 1.78° , and in the horizontal range between the target and the rail, which increases by 0.98 m. To address the effects associated with each of the two changes independently, the cylinder oriented at 0° with respect to the rail is considered, and two separate simulations are carried out: one in which the height of the source and receive array is changed so as to reproduce the change in grazing angle, and one in which the grazing angle is kept constant and the horizontal range, and consequently also the source and receive array height, are changed. Fig. 15 shows the result of these computations in comparison with the broadside insonification case for the tower in the same position as the experiment, and in comparison with the data. The target strength appears to be sensitive mainly to small changes in the grazing angle. Figs. 12–14 suggest that the actual source-target-receiver geometry of the experiment should be taken into account by the numerical model. Nevertheless, some discrepancies such as the null near 10 kHz or the low target strength levels between 15 and 20 kHz appear to be stable with respect to variations in the geometry.

In the examples of Figs. 12–14, the Green's function used in the model is the second order accurate approximation resulting from the steepest descent approximation of the wavenumber spectral integral (Eqs. (4)–(6) in Zampolli et al.⁵). In this approximation, the Green's function is described by a direct free field point source and an image point source premultiplied by an effective reflection coefficient that accounts for the spectra of plane waves contributing to the fields realized for finite source/receiver geometries. An additional lateral wave contribution, originating from a branch point contribu-

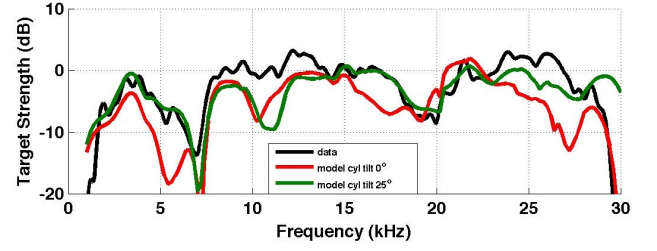


FIG. 14: Computed target strength for broadside insonification, obtained by two different combinations of cylinder orientation relative to the rail and tower displacement.

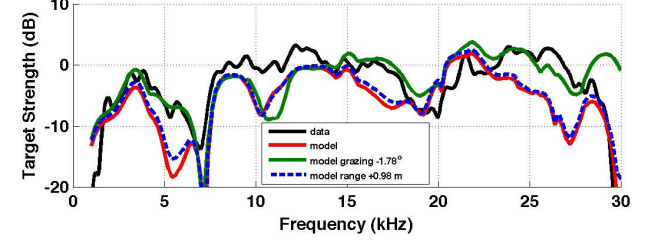


FIG. 15: Sensitivity of the beamformed array response to changes in the grazing angle (keeping the range constant), and to changes in the range (keeping the grazing angle constant), for broadside insonification and cylinder orientation 0° with respect to the rail.

tion in the integrand of the spectral wavenumber representation, is also taken into account. The first order accurate approximation, instead, considers only the direct free field point source and the image source multiplied by the plane-wave reflection coefficient associated with the grazing angle of the ray connecting the image source and the source point of the Green's function. Figure 16 shows the comparison between the model results obtained by the FE model with second order accurate Green's functions, and by the same model using the first order accurate Green's functions. The two computed target strength curves are virtually identical across most of the frequency band, with the first order approximation exhibiting a better agreement with the experimental data at the lower frequencies. The first order accurate Green's function can be obtained from the second order accurate one by omitting the correction term in the reflection coefficient, $-iN/(kR_1)$ in Eq. (4) of Zampolli⁵, and by omitting the lateral wave contribution, Eq. (6) in that same reference. Eliminating the two terms one at a time, and performing the comparison between the numerical results obtained, shows that the second order correction to the reflection coefficient is negligible in the cases considered here, and that the lateral wave contribution does not appear to be visible in the experimental results.

The model described in this section is used to compute the target strength as a function of azimuth and frequency for the same cylinder orientation angles and source aspect angles as those used to produce the exper-

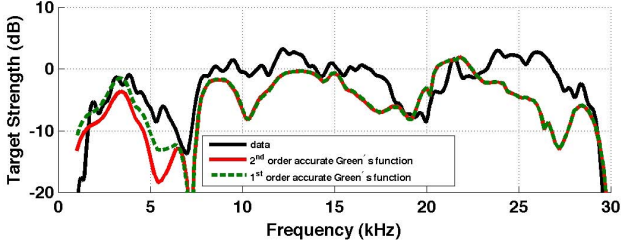


FIG. 16: Computed target strength for broadside insonification, obtained using different approximations of the layered medium Green's function. The first order accurate Green's functions are the same as those used in Sec. IV A.

imental results of Fig. 4. The vertical array tilt angle is the same as in the experiment, and the array responses are broadside beamformed. The results are shown in Fig. 7 for the model with second order accurate layered medium Green's functions, and in Fig. 8 for the same model with the first order accurate Green's functions. Comparison of the results shows that the consideration of the experimental source-target-receiver geometry contributes to improving the model-data agreement, particularly in the region between 15 and 30 kHz, with azimuthal angles from 10 to 80 degrees. Using the first order approximation of the layered medium Green's function improves the model-data agreement at low frequencies.

A more detailed look at model/data comparisons for a few angles is shown in Fig. 17. Much of the structure seen in the data is also reproduced in both the model of Sec. IV A and the present section. The comparisons indicate that the models capture much of the important physics. However, given that the discrepancies in the nulls around 10 kHz and 20 kHz for broadside and near-broadside angles (Figs. 12–14) are insensitive to variations in the source-target-receiver geometry, there is a need to address the acoustic interaction with the sediment with more accurate models. In particular a three-dimensional finite element model that takes into account the contact surface between the target and the sea floor, and a more accurate model of the sea floor reflection coefficient as a function of angle and frequency are two avenues for further effort. The first of these avenues is addressed in the next section.

C. Three dimensional finite element analysis

The analysis is steady-state, a.k.a. cw or frequency-domain, with the time-frequency dependence being $e^{+i\omega t}$. Spatially, the analysis is divided into two regions: (i) a finite target region, consisting of the target surrounded by a small ball of fluids, and (ii) the infinite region exterior to the target region. For each frequency/aspect-angle pair of values, the analysis comprises two steps: (i) the scattered field is first computed in the target region and (ii) that solution is then used to compute the scattered

field exterior to the target region.

Scattering in the target region is modeled using the commercial finite-element (FE) software Comsol Multiphysics¹⁸, complemented by several novel FE modeling techniques developed at the Naval Surface Warfare Center, Panama City Division (NSWC PCD) for significantly increasing computational efficiency. Scattering in the exterior region is modeled using non-FE analytical techniques, also developed at NSWC PCD¹⁹.

1. Target Region

The target region has three subdomains (Fig. 18): (i) a hemisphere of water, (ii) a hemisphere of sediment, modeled as a fluid, and (iii) a solid aluminum cylinder, with its axis parallel to the interface and lying almost entirely in the water but slightly buried (0.005 m deep) in the sediment. The hemispherical outer boundaries are located 1.5 wavelengths from the cylinder at all frequencies. Second-order Bayliss Turkel radiation absorbing boundary conditions²⁰ are applied on the hemispherical boundaries, which approximate infinite half spaces to within a modeling error of typically one or two percent.

The governing PDE in the cylinder is the linear elastodynamic equation for viscoelastic, anisotropic, inhomogeneous solids,

$$-\nabla \cdot (\mathbf{c} \nabla \mathbf{u}) - \omega^2 \rho_s \mathbf{u} = 0 \quad (2)$$

where \mathbf{u} is particle displacement, \mathbf{c} is a 4th-rank tensor of elastic moduli and ρ_s is solid density.

The governing PDE in the fluids is the linear Helmholtz equation for inviscid (though including bulk attenuation), anisotropic, inhomogeneous fluids,

$$-\nabla \cdot \left(\frac{1}{\omega^2 \rho_f} \nabla p \right) - \frac{1}{B} p = 0 \quad (3)$$

where p is the *scattered* acoustic pressure (defined below), ρ_f is fluid density, B is bulk modulus, and the operand of the divergence operator (the “flux”) is particle displacement,

$$\mathbf{u} = \frac{1}{\omega^2 \rho_f} \nabla p \quad (4)$$

Although the water and the sediment are modeled as homogeneous fluids with different densities, Eq. (3) treats both fluids together as a single inhomogeneous fluid with a piecewise-constant density. A single dependent variable p therefore applies to both fluids, with continuity of p and normal particle displacement [normal component of Eq. (4)] automatically enforced on fluid-fluid interfaces as Dirichlet and Neumann conditions, respectively, during element assembly.

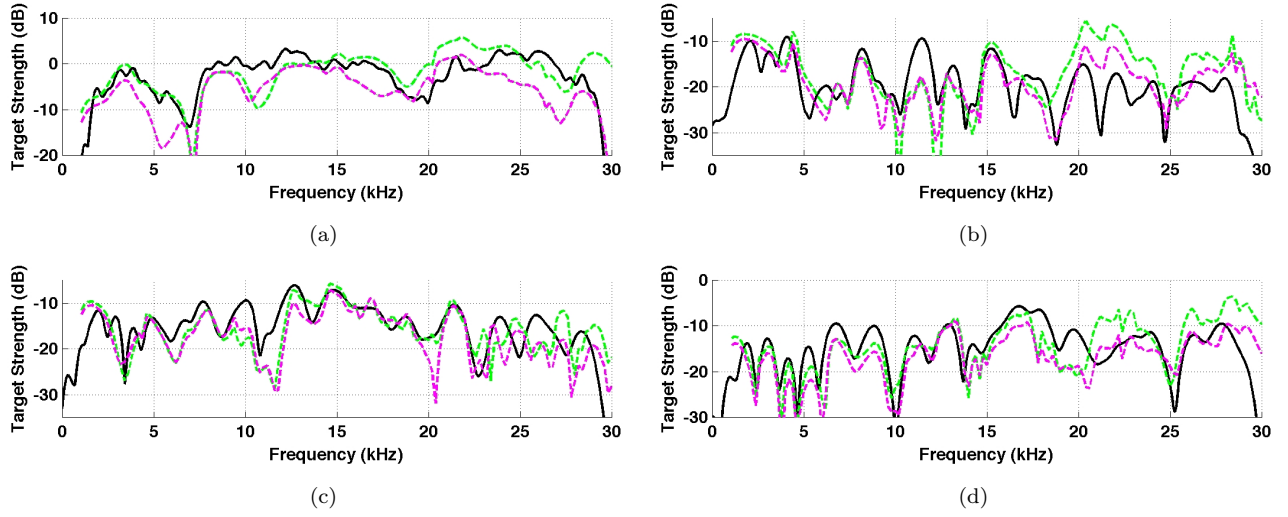


FIG. 17: Comparisons of data (black), finite element results using plane wave incident and scattering angles (green), and finite element results using experimental geometry with first order accurate Green's function (magenta): a) broadside, b) 17° relative to broadside, c) 23° relative to broadside, d) 33° relative to broadside.

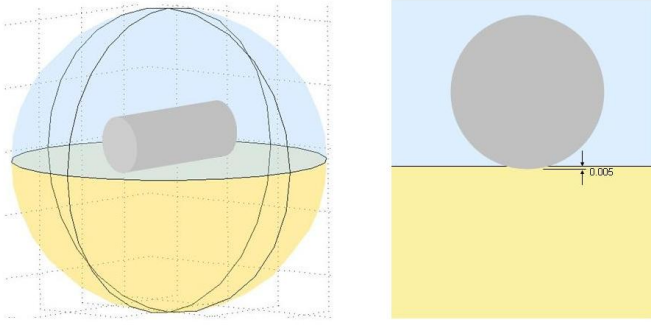


FIG. 18:

Left: Geometry of FE model for target region, Right: enlarged end view of cylinder.

Placing ω^2 in the denominator of the divergence operand, rather than in the numerator of p/B as is often done in acoustics, is important in *structural* acoustics because it yields symmetric fluid-solid FE coupling matrices; therefore the entire FE matrix system is symmetric. This symmetry is a manifestation of reciprocity, which characterizes linear fluid and solid media.

The scattered field, p , is defined as the field remaining after subtracting the incident field from the total field,

$$p = p^{total} - p^{inc} \quad (5)$$

where the incident field, p^{inc} , is, by definition, the field that would exist in the absence of the target. The physical incident field for this analysis is assumed to be a plane wave. The analytical field p^{inc} is therefore the well-known theoretical solution for a plane wave incident on the interface of two fluid halfspaces, i.e., incident and reflected plane waves in the water and a transmitted plane

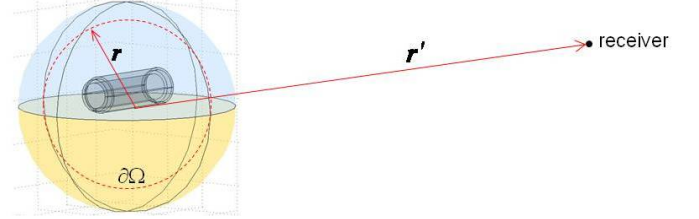


FIG. 19:

Geometric meaning of variables used in Helmholtz integral.

wave in the sediment²¹.

2. Exterior to the target region

Target strength is computed at the center of the experimental receive array. The array is over 9 m away, which is well outside the FE target region, even at the lowest frequencies. Therefore, the field exterior to the target region is computed using the Helmholtz (a.k.a. Helmholtz-Kirchoff) integral,

$$p(\mathbf{r}') = \int \int_{\partial\Omega} \left(\frac{\partial G(\mathbf{r}', \mathbf{r})}{\partial n} p(\mathbf{r}) - G(\mathbf{r}', \mathbf{r}) \frac{\partial p(\mathbf{r})}{\partial n} \right) d\Gamma \quad (6)$$

where $\partial\Omega$ is any closed surface circumscribing the target (Fig. 19), n is the outward unit normal to $\partial\Omega$, \mathbf{r} is the location of $d\Gamma$ on $\partial\Omega$, \mathbf{r}' is the location of the receiver, $G(\mathbf{r}', \mathbf{r})$ is the Green's function for the environment, i.e., two infinite halfspaces, $p(\mathbf{r})$ is the scattered field computed in the FE analysis of the target region, and $p(\mathbf{r}')$ is the desired scattered field at the receiver.

The NSWCD PCD 3-D FE system offers two analytical methods for computing $G(\mathbf{r}', \mathbf{r})$: (i) wavenumber integration, which is an exact formulation but computationally slow, and (ii) a steepest-descent approximation to the wavenumber integration, which assumes the receiver is many wavelengths from the target but is computationally fast²². The results below used the steepest-descent method because the two methods, randomly sampled, differed by only about 1 percent.

3. Uniform modeling error across entire frequency band

Acoustic response as a function of angle and frequency is not an end in itself; it is usually input to detection and classification signal-processing algorithms. The accuracy of those algorithms is significantly increased if the modeling error in the FE calculation is uniform across the entire frequency band. The NSWCD PCD software system achieves this by scaling the target-region FE models in two ways: (i) the outer fluid boundaries are located a constant number of incident wavelengths (1.5 in this analysis) from the cylinder at all frequencies, and (ii) the number of finite elements per incident wavelength, in all directions, is maintained constant at all frequencies. The NSWCD PCD software system automatically controls this scaling.

4. Results

Target strength: Figure 9 is the complete broadband multi-aspect acoustic plot. Target strength was computed every 0.1 kHz from 1 to 30 kHz and every 0.5 degrees from 0 to 90 degrees, a total of 54,481 3-D models. Using an exact (no approximations introduced) symmetry-based domain decomposition technique, each of the 54,481 3-D models was reduced to one quadrant of the geometry in the left panel of Fig. 18. Each quadrant was analyzed four times, each time with a different excitation and different boundary conditions, and the four results were then added. Thus, there was a total of 217,924 3-D FE quadrant analyses. Using quadratic elements throughout the domain, the computational size of the quadrant analyses ranged from 10K degrees of freedom (dof) at 1 kHz to 813K dof at 30 kHz. The complete acoustic plot took about 30 hours on a 25-blade distributed processing system with two dual-core 3 GHz processors per blade.

This should be compared with the experimental data in Fig. 4. A more precise comparison is shown in Fig. 20, which plots the horizontal slices at 0° azimuthal angle (broadside) from both Fig. 9 and Fig. 4.

Figure 20 indicates that most of the experimental/numerical differences are in the range of about 2 to 5 dB. This is quite reasonable, perhaps even better than to be expected, when one considers both the experimental and numerical errors.

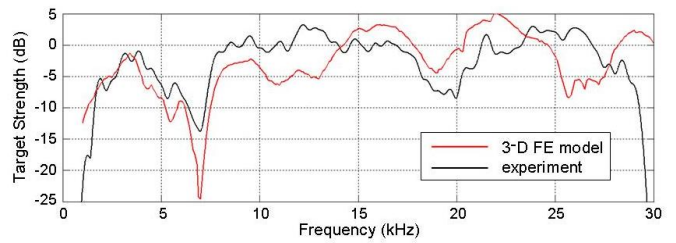


FIG. 20:

Comparison of 3-D FE model and experimental data at broadside insonification.

On the experimental side, measurements of this type typically have several sources of error, which, collectively, usually amount to about 2 to 3 dB.

On the numerical side, three intentional approximations were made. First, the incident field in the model is a plane wave, i.e., the source at infinity, which yields a single grazing angle. In the experiment the source is a transmitter about 10m from the cylinder, which insonifies the cylinder with almost-plane waves with a range of grazing angles. Second, target strength in the model is computed at a single point, the center of the receive array, whereas the experiment physically integrates the scattered field over each of the arrays six elements and the electronics beamform the six outputs. Last, the model treats the sediment as an ideal acoustic fluid (with dissipation), ignoring the granularity of the sand-water mixture.

A fourth source of numerical error is discretization error, which is inherent in any FE model. However, the next section shows that that error is negligible in this model.

Discretization error: Figure 21 shows the results of a convergence study. The red curve is the same as the red curve in Fig. 20. The green curve is the result of enriching all the quadratic elements to cubic elements; it stops at 20.5 kHz because at that frequency the model contains over one million degrees of freedom, which is close to the limit for an in-core solution. A numerical comparison of the two curves reveals that (i) the mean discretization error is about 0.15 dB, and (ii) the discretization error is quite uniform over the tested band of 1 to 20.5 kHz, as predicted in Sec. IV C 3.

V. SUMMARY AND DISCUSSION

An experiment examining scattering from an aluminum cylinder placed proud on a water/sand interface has been described and results shown. Those results were compared to finite element calculations that included different assumptions. The model/data comparisons show first and foremost that the inclusion of the environment (in this case the water/sediment interface) is essential for accurately predicting the cylinder's target strength as a

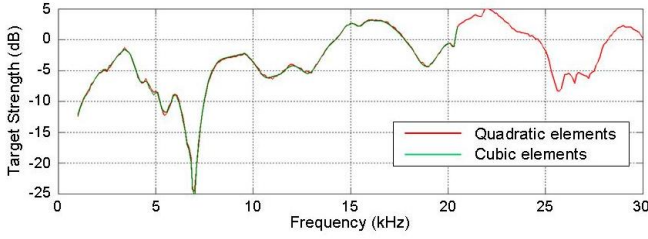


FIG. 21:

Comparison of the FE model results at broadside insonification using quadratic (red) and cubic (green) elements.

function of frequency and angle.

The finite element modeling was carried out in three ways. The first model involved use of multiple 2-D finite element calculations for scattering from the cylinder in the freefield assuming plane wave incidence and a single scattering angle (receiver at infinity). This was combined with the use of image cylinders to treat the scattering from the sand/water interface. The second model also used 2-D finite element calculations but used the geometry of the experiment, summed the returns calculated at each receiver element and used a more accurate two fluid Green's function. The second model demonstrated the sensitivity of data/model comparisons to the experimental geometry.

Neither of the first two models accounted for multiple scattering that can occur between the cylinder and the sand/water interface. The last model addressed this deficiency via use of a fully 3-D finite element method with the source at infinity (plane wave incidence) but the (point) receiver at a finite distance. This model also holds the promise of treating much more complicated targets and waveguide propagation. A future step will be to include the experimental geometry in the 3-D modeling.

From at least an overall qualitative standpoint the 3-D model seems to more accurately capture the target strength behavior for the region identified in previous sections as including contributions from helical waves (frequencies of 15 to 30 kHz with azimuthal angles from 10 to 20 degrees, cf. Fig. 4 to Fig. 9). As noted earlier, this particular region has the potential to be more significantly impacted by the fact the cylinder is in contact with the sediment. More quantitatively, Figure 22 shows the same angles as Fig. 17 but with model results separated so that model/data comparisons for each model can be more clearly seen. Generally speaking, each model has particular frequency/angle regions where it is closest to the data.

Differences between models and between data and models are as much as a few dB. However, the over all target strengths as well as the structure seen both as a function of frequency and angle is sufficient to demonstrate the ability of finite element modeling to capture the response of the target. In the future a model-to-model comparison of the second and third models, where

the experimental geometry is more accurately treated in the 3-D model, should be useful in isolating any multiple scattering effects.

The level of detail captured by the finite element modeling is indicative of the high fidelity possible via these type of calculations. However, understanding the basic physical phenomena that are responsible for the features seen required the insight derivable from complementary physical acoustics modeling. For instance, the dip seen in broadside target strength (for the data and all models) around 7 kHz can be shown to be a direct result of, and very sensitive to, the the phase of the water/sediment reflection coefficient. Also, the fact that the major contributors to the target strength measured near $\phi = 90^\circ$ are the bistatic paths including a single reflection from the water/sediment interface, is something easily argued via physical acoustics and proven true using the image cylinder model by examining the separate contributions. In the end, insights derived using the combination/comparison of experiment, physical acoustics and finite element modeling may be essential in understanding and predicting the changes caused by the environment and an object's orientation within that environment.

Appendix A: Geometry and angle definitions for Sec. IV A

The goal is to translate the rotations of the cylinder around an axis normal to the plane of the water/sediment interface into the coordinate system defined for the finite element calculations^{5,6}. That this translation is required can be seen by considering a cylinder rotation in the plane of the water/sediment interface (the defining angle of the experimental results in Fig. 4) from broadside (0°) to end on (90°). Since the source and receiver are above this plane there is never an end-on geometry realized in the experiment. This translation is also needed in order to calculate the bistatic scattering contribution from the image cylinder associated with the single reflection off the water/sediment interface.

Figure 23 defines the geometry needed to obtain the angles required for the finite element calculation (θ_{cyl} and ϕ_{cyl}) in terms of those of the experiment (θ_g and ϕ). Implicit in these definitions is that the source and receiver are at $-\infty$ with an associated grazing angle onto the cylinder and the sediment of θ_g . Also, though the experiment uses a combination of cylinder orientations and movement of the source and receiver along a rail, here the situation is examined as though the source and receiver are stationary and the cylinder rotates through a continuous set of angles ϕ .

From Fig. 23 the following equations can be determined:

$$\hat{z}_{cyl} = \sin \phi \hat{x} + \cos \phi \hat{y}, \quad (A1)$$

$$\hat{r}_{sr} = \sin \theta_g \hat{z} - \cos \theta_g \hat{x}, \quad (A2)$$

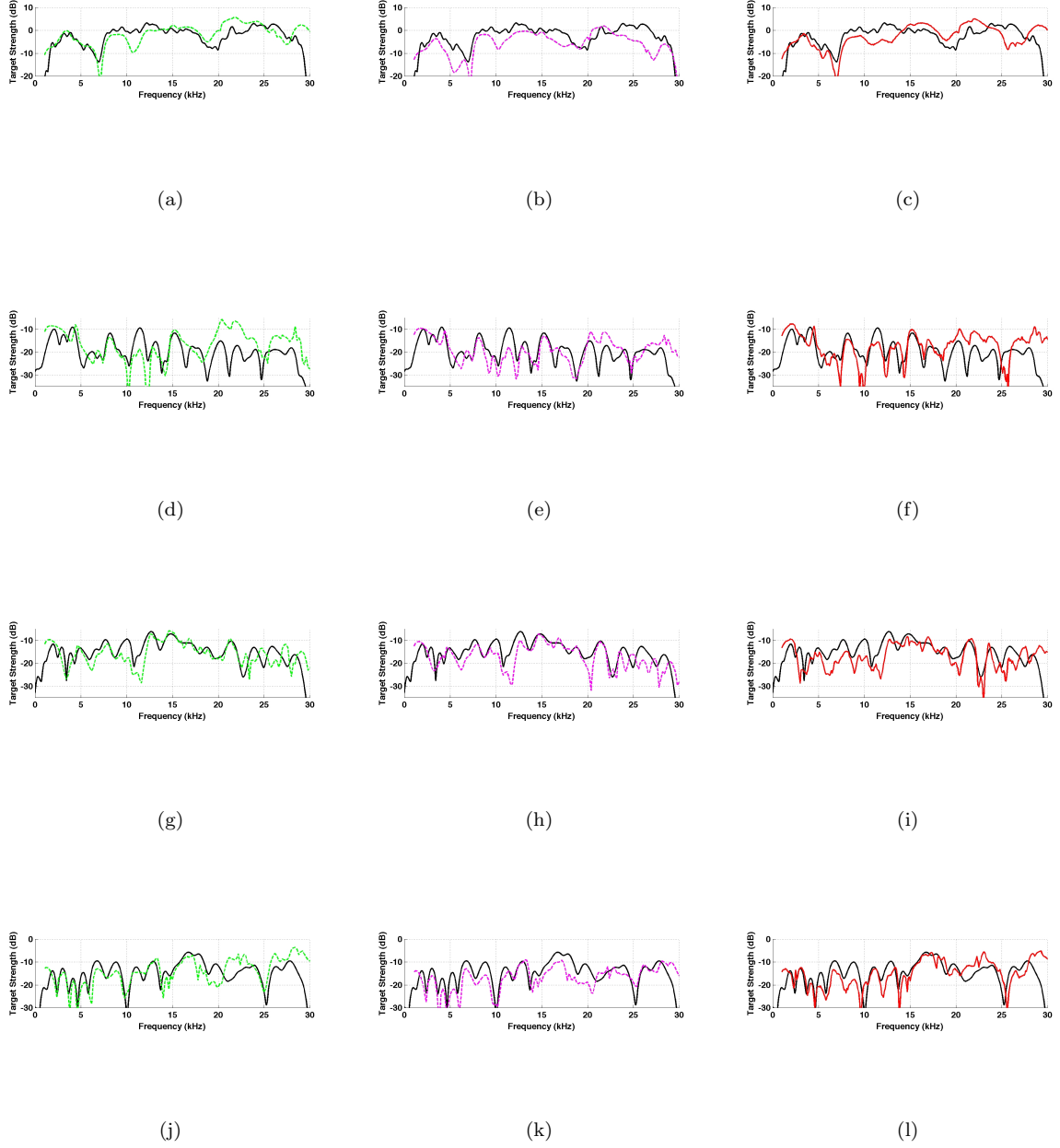


FIG. 22: Comparisons of data (black), finite element results using plane wave incident and scattering angles (left column, green curves), and finite element results using experimental geometry with first order accurate Green's function (center column, magenta curves), 3-D finite element results (right column, red curves): top row) broadside, top center row) 17° relative to broadside, bottom center row) 23° relative to broadside, bottom row) 33° relative to broadside.

$$\hat{\mathbf{r}}_{sr} = \cos \phi_{cyl} \hat{\mathbf{r}}_{cyl} - \sin \phi_{cyl} \hat{\mathbf{z}}_{cyl}, \quad (\text{A3}) \quad \text{and}$$

where $\hat{\mathbf{z}}_{cyl}$ is the unit vector along the cylinder axis and $\hat{\mathbf{r}}_{sr}$ is the unit vector pointing toward the source and receiver.

From Eqs. (A1), (A2), and (A3) one has

$$\hat{\mathbf{z}}_{cyl} \cdot \hat{\mathbf{r}}_{sr} = -\sin \phi_{cyl}, \quad (\text{A4})$$

$$\hat{\mathbf{z}}_{cyl} \cdot \hat{\mathbf{r}}_{sr} = -\cos \theta_g \sin \phi. \quad (\text{A5})$$

From (A4) and (A5) one gets the first of the relations sought, i.e.,

$$\phi_{cyl} = \arcsin(\cos \theta_g \sin \phi). \quad (\text{A6})$$

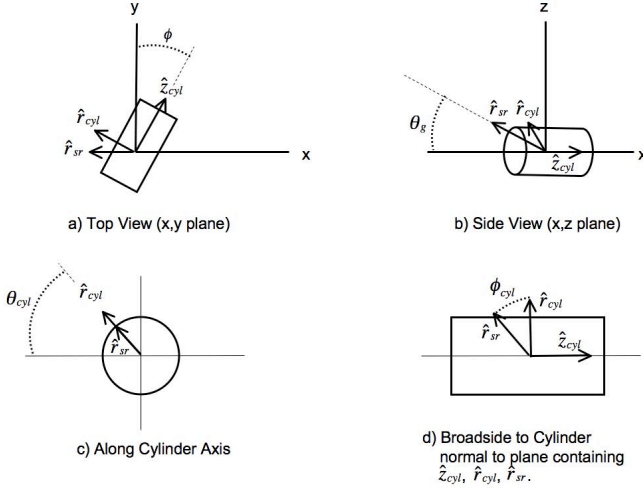


FIG. 23:

Definition of angles and unit vectors needed to get θ_{cyl} and ϕ_{cyl} in terms of θ_g and ϕ

Eqs. (A1)–(A3), and (A6) can also be used to get an expression for \hat{r}_{cyl} in terms of θ_g , ϕ , \hat{x} , \hat{y} , and \hat{z} :

$$\hat{r}_{cyl} = \frac{1}{\sqrt{1 - \cos^2 \theta_g \sin^2 \phi}} \times \quad (A7)$$

$$(-\cos \theta_g \cos^2 \phi \hat{x} + \cos \theta_g \sin \phi \cos \phi \hat{y} + \sin \theta_g \hat{z}).$$

The relation for θ_{cyl} comes from the dot product of (A7) with the unit vector perpendicular to \hat{z}_{cyl} in the x-y plane, $-\cos \phi \hat{x} + \sin \phi \hat{y}$, giving

$$\theta_{cyl} = \arccos \left(\frac{\cos \phi \cos \theta_g}{\sqrt{1 - \cos^2 \theta_g \sin^2 \phi}} \right). \quad (A8)$$

Acknowledgments

Work supported by the Office of Naval Research and the Strategic Environmental Research and Development Program (SERDP) program.

DSB wishes to acknowledge the following contributors to the 3-D FE modeling effort in Sec. IV: Mr. Les Wigdor for his integration of FE and non-FE modeling systems into a user-friendly GUI-driven 3-D FE system, Dr. Gary Sammelmann for his non-FE analytical techniques for scattering in the exterior region, and Mr. Darshan Bryner for his mathematical support and execution of the many FE models in a distributed-processing environment.

- ¹ R. Lim, K. L. Williams, and E. I. Thorsos, “Acoustic scattering by a three-dimensional elastic object near a rough surface,” *J. Acoust. Soc. Amer.* **107**, 1246–1262 (2000).
- ² A. Tesei, A. Maguer, W. L. J. Fox, R. Lim, and H. Schmidt, “Measurements and modeling of acoustic scattering from partially and completely buried spherical shells,” *J. Acoust. Soc. Amer.* **112**, 1817–1830 (2002).
- ³ J. L. Lopes, C. L. Nesbitt, D. T. R. Lim, K. L. Williams, and E. I. Thorsos, in *Proceedings of Oceans 2002 MTS/IEEE* (PUBLISHER, Biloxi, Mississippi, 2002), pp. 461–467.
- ⁴ J. A. Fawcett and R. Lim, “Evaluation of the integrals of target/seabed scattering using the method of images,” *J. Acoust. Soc. Amer.* **114**, 1406–1415 (2003).
- ⁵ M. Zampolli, A. Tesei, G. Canepa, and O. A. Godin, “Computing the far field scattered or radiated by objects inside layered fluid media using approximate Green’s functions,” *J. Acoust. Soc. Amer.* **123**, 4051–4058 (2008).
- ⁶ M. Zampolli, A. Tesei, F. B. Jensen, N. Malm, and J. B. Blottman, “A computationally efficient finite element model with perfectly matched layers applied to scattering from axially symmetric objects,” *J. Acoust. Soc. Amer.* **122**, 1472–1485 (2007).
- ⁷ S. K. Numrich, V. V. Varadan, and V. K. Varidan, “Scattering of acoustic waves by a finite elastic cylinder immersed in water,” *J. Acoust. Soc. Amer.* **70**, 1401–1411 (1981).
- ⁸ X.-L. Bao, “Echoes and helical surface waves on a finite cylinder excited by sound pulses in water,” *J. Acoust. Soc. Amer.* **94**, 1461–1466 (1993).
- ⁹ K. Gipson and P. L. Marston, “Backscattering enhancements due to reflection of meridional leaky Rayleigh waves at the blunt truncation of a tilted solid cylinder in water: Observations and theory,” *J. Acoust. Soc. Amer.* **106**, 1673–1680 (1999).
- ¹⁰ K. Gipson and P. L. Marston, “Backscattering enhancements from Rayleigh waves on the flat face of a tilted solid cylinder in water,” *J. Acoust. Soc. Amer.* **107**, 112–117 (2000).
- ¹¹ B. T. Hefner and K. L. Williams, “Sound speed and attenuation measurements in unconsolidated glass-bead sediments saturated with viscous pore fluids,” *J. Acoust. Soc. Amer.* **120**, 2538–2549 (2006).
- ¹² D. R. Jackson and M. D. Richardson, in *High-Frequency Seafloor Acoustics* (Springer, New York, NY, 2006), p. 251.
- ¹³ P. L. Marston, “Approximate meridional leaky ray amplitudes for tilted cylinders: End-backscattering enhancements and comparisons with exact theory for infinite solid cylinders,” *J. Acoust. Soc. Amer.* **102**, 358–369 (1997).
- ¹⁴ K. Baik, Ph.D. thesis, Washington state University, Pullman, WA, 2008.
- ¹⁵ P. L. Marston, in *Acoustical Imaging*, edited by S. Lees and L. A. Ferrari (Plenum, New York, 1997), pp. 369–374.
- ¹⁶ K. Baik and P. L. Marston, “Kirchhoff approximation for a cylinder breaking through a plane surface and the measured scattering,” *IEEE J. Ocean. Eng.* **33**, 386–396 (2008).
- ¹⁷ J. Shirron, private communication (unpublished).
- ¹⁸ Comsol Multiphysics User’s Guide, Version 3.4 (2007).
- ¹⁹ G. Sammelmann, private communication (unpublished).

- ²⁰ A. Bayliss, M. Gunzberger, and E. Turkel, “Boundary conditions for the numerical solution of elliptic equations in exterior regions,” *SIAM J. Appl. Math.* **42**, 430–451 (1982).
- ²¹ F. B. Jensen, W. A. Kuperman, M. B. Porter, and H. Schmidt, in *Computational Ocean Acoustics* (AIP Press, New York, NY, 1994), Chap. 1.6.1.
- ²² L. M. Brekhovskikh, in *Waves in Layered Media* (Academic Press, New York, NY, 1960), Chap. 19.